Modulating coalescence timing of liquid marbles via wettability adaptation

Chittaranjan Mishra, [a] Debasmita Sarkar,[a] Nishanta Barman, [a] Saurav Kumar, [a] Mizuki Tenjimbayashi* [b] and Uttam Manna*[a,c,d]

[*][a] Department of Chemistry, Indian Institute of Technology-Guwahati, Assam, 781039 India. E-mail: umanna@iitg.ac.in
[*][b] Research Center for Materials Nanoarchitectonics (MANA), National Institute for Materials Science (NIMS), Tsukuba, Ibaraki, Japan
E-mail: TENJIMBAYASHI.Mizuki@nims.go.jp
[c]Centre for Nanotechnology, Indian Institute of Technology-Guwahati, Assam, 781039 India.
[d] Jyoti and Bhupat Mehta School of Health Science & Technology, Indian Institute of Technology-Guwahati, Assam, 781039 India.

Keywords: Automated coalescence • wettability adaptation • liquid marble • chemical modifications • 1,4-conjugate addition reaction

Abstract

Droplet coalescence is ubiquitous in nature, and its regulation is significant in industrial processes and biomedical applications. While bare droplets suddenly coalesce in contact, the droplets covered with liquid-repellent particles to form "liquid marbles (LMs)" are not. Previously, the external stimuli-responsive breakage of the particle layer enabled the regulation of the coalescence timing. However, preprogramming the coalescence timing of droplets without stimuli is challenging. In this work, we report LMs that break the particle layer in preprogrammed time. The particles have a core wettable site and are tethered with a low-wettability flexible molecular chain, which gradually increases wettability with time. The time-dependent wettability variation is observed because of the differences in the adaptation of the molecular chain; thus, it is repeatedly available, and its speed is controllable by chain length. The formed LMs expose bare droplet surfaces in preprogrammed timing, which enables the modulation of coalescence timing from 2 to 45 minutes without relying on external stimuli. Moreover, the additivity of the particles enabled the fine-tuning of the coalescence time with ~ 1-minute resolutions. Further, the contact of several LMs with different adaptation times enabled cascade droplet coalescence, opening a new route for droplet manipulation.

Introduction

Liquid marbles (LMs) are non-sticking droplets derived by coating a millimetric water droplet with hydrophobic micro/nano-particles. It provides a facile basis to protect the encapsulated water droplet from mass loss because of adhesion to a solid surface and undesired contamination while subjecting to effortless rolling or other physical manipulation on a solid surface.[1-3] Because of these features, LMs appeared as prospective materials for a wide range of applications—including tissue engineering,[4-7] miniaturized chemical reactions,[8-11] single-cell picking,[12] chemical sensing,[13-15] and actuators.[16-19] For realizing these applications, manners of coalescing LMs are often required. [4-19] In the past, either re-arrangements of hydrophobic particles around the encapsulated water droplet [4,8-9,20,21] or alteration of water repellence of selected particles under an adequate external stimulus [22,11] enables the coalescence of LMs on solid surfaces. For instance, the coalescence of LMs was demonstrated by colliding them with external mechanical force [4,23,24], where LMs often fail to sustain such mechanical impact, damaging the physical integrity of LMs. As an alternative approach, LMs were subjected to an external electric field at high operating voltage to achieve electro-coalescence by forming a liquid bridge across the LM shell. [8,25,26] Later, responsive LMs were introduced to achieve their coalescence by selectively melting thermo-responsive constituents of the LM shell.[27] Even the strategic association of hydrophobic particles with magnetic nanoparticles allows LMs coalescence under an external magnetic field.[9,28] Moreover, a systematic increase in the volume of the inner liquid of LMs provided an active LM shell with unjammed particles, enabling their coalescence on contact.[20] While this, particles embedded with stimuli (i.e., UV light or CO_2 gas) responsive water repellence also display the coalescence of LMs in the presence of appropriate stimuli.[11,22] Thus, all these earlier reported approaches demand an adequate external intervention to depict the coalescence of LMs. The challenge is an automated coalescence of LMs with absolute control over coalescence timing, where no external interventions are required.

Here, we demonstrated the automated coalescence of LMs through wettability adaptation of the prepared hydrophobic particles from Cassie to Wenzel states. The developed LMs were chemically programmed to release the inner liquid on the hydrophilic substrate (i.e., bare glass surface) at a pre-set time (referred to as LM lifetime), where the transition of water wettability of prepared particles from Cassie to Wenzel states depends on the chemical modifications—and their adaptation to water. More precisely, the adaption time gradually increases with the carbon chain length of the selected modifiers—i.e., alkyl amines utilized in preparing the hydrophobic particles. Such LMs enabled automated coalescence by forming a liquid bridge when placed on a superhydrophobic substrate, as shown in Scheme 1. Particles

with different chemical modifications were mixed at different proportions to tailor the coalescence time from 2 to 45 minutes, where adaptation speed on the molecular scale and Cassie-Wenzel transition speed at the particle scale contribute to modulating the coalescence time between LMs (Scheme 1). The mixing of the inner liquids of multiple LMs can be efficiently sequenced at a pre-set time frame to perform cascade chemical reactions.

Results and Discussions

In our current design, we prepared a reactive nanoparticle (NP) from bovine serum albumin (BSA) and dipentaerythritol penta-acrylate (5-Acl) to introduce adaptive wettability (Figure 1A). To prepare reactive NP, we adopted the desolvation process [29] and covalent crosslinking chemistry with dipentaerythritol penta-acrylate (5-Acl), where residual acrylate moiety present in the prepared nanoparticles enables the surface modification with primary amine-containing selected small molecules, i.e., different alkyl amines with carbon chain length (n) ranging from n = 3 to 18 (Figure 1A). The field emission electron microscope (FE-SEM, Figure 1B) revealed the globular morphology of the reactive NP (size of 65±16 nm, Figure S1), and the existence of residual acrylate groups in the reactive NP was validated with FT-IR analysis (Figure 1C). While the characteristic IR signatures for the amide-I band and amide-II band at 1648 cm^{-1} and 1535 cm^{-1} appeared because of BSA protein [30], additional IR signatures for the vinylic C–H and C=O stretching at 1410 cm^{-1} and 1736 cm^{-1}, respectively, suggested the presence of residual acrylate groups in the prepared reactive NP. On its further post-chemical modification with octadecyl amine (n = 18), the IR signature at 1410 cm^{-1} was significantly and selectively depleted, comparing an invariable IR signature at 1736 cm^{-1}. Such chemical modification has minimal impact on its morphology, as confirmed by FE-SEM images (Figure 1B). This study suggests that the structural integrity of the reactive BSA NPs remains unaffected despite incorporating the long chain of octadecyl groups. However, such chemical modification certainly improves its water repellency. While water droplets beaded on the powder bed of reactive NPs with a water contact angle (θ_w) of 0°, after chemical modification with octadecyl amine, it exhibited superhydrophobicity with θ_w of 159° (Figure 1D).

The prepared reactive NP provides diverse water wettability through modification with different alkyl amines, ranging from propyl amine (n = 3) to octadecyl amine (n = 18), as shown in Figure 2A. As the carbon chain length n increases, the θ_w elevates, ultimately achieving superhydrophobicity for $n \geq 6$ (Figure-2A, Figure S2, supporting information). Thereafter, the adaptation of modified NP towards water was studied by measuring the θ_w of a beaded water droplet on a powder bed with time (Figure S3, supporting information). The change in the

cosine component of the θ_w with the time t for different modifications reveals a faster wettability adaptation by NP modified with a short-chain alkyl group (Figure 2B). The faster adaptability of the short-alkyl chain modified NP compared to long-alkyl chains is further schematically depicted in Figure 2C. On the molecular scale, water can readily infiltrate through a short-alkyl chain—i.e., propyl moiety to reach out to a hydrophilic NP core made of BSA. Eventually, the water wettability on the modified NP (n = 3) powder bed surface improved significantly (θ_w decreased from 140° to 96° within 30 minutes). In contrast, NP modified with a long-hydrocarbon chain (n = 18) restricts the water ingression through it. Consequently, a minimal change in water wettability was noticed after 30 minutes for the NP modified with long alkyl moiety (n = 18).

Figure 2D extracted the contact angle evolution from Figure 2B, in which two trends of the decrease in contact angle can be found. At the initial state, the contact angle variation speed is slow (see the red fitting slope in Figure 2D) because the NP−water contact area near the contact line is small, Cassie contact (Figure 2D). However, the variation speed gradually increases with t, which can be explained by increasing the contact area by invasion of the water between the NPs (Figure 2E). Finally, the water layer is entirely trapped between NPs to form Wenzel contact (see green fitting slope in Figure 2D). Thus, we consider the contact angle variation dependent on the NP−water contact area, which is depicted in the schematics in Figure 2E. Then, we quantify the wetting adaptation speed from the decreasing speed of the contact angle (Figure 2D). We developed the Malthusian growth model for wettability adaptation, namely the Malthusian contact model. This model considers the hydrophilization rate β to be proportional to the current NP−water contact area, which is based on the following assumptions: (1) hydrophilization speed per unit NP−water contact area is constant; (2) the contact area increases with $\cos\theta$; (3) $\cos\pi$ is the case of the contact area being zero. The model equation is expressed to be $\frac{d(\cos\theta-\cos\pi)}{dt} = \beta(\cos\theta - \cos\pi)$. By solving this, we finally obtain

$$\cos\theta = -1 + (\cos\theta_0 + 1)e^{\beta t} \quad (1)$$

, where θ_0 is the initial water contact angle on the NP powder bed surface. Equation (1) worked well (coefficient of determination is R^2 = 0.97) to explain the contact angle evolution (see the blue fitting curve in Figure 2D). Please note that the contact angle becomes constant after reaching the equilibrium. Thus, this model is expected to be available only when the surface wettability of the nanoparticles to water increases with time. The potential expandability is the wetting analysis of the adaptive materials.[31] Figure 2B offered the adaptation rate for different alkyl chain lengths by fitting Equation (1) (Figure S4, supporting information). As a result, we obtained their inverse proportion (Figure 2F):

$$\beta \sim n^{-1} \quad (2)$$

The relationship is consistent with our estimation that the longer alkyl chain delays the adaptation speed. It is worth mentioning that the adaptation rate increases with elevating the humidity for a modified NP, as shown in Figure S5.

Although the NP decorated with propyl moiety (n = 3) displayed a sharp decrease in θ_w from 140° to 40° within 60 minutes (Figure S3, supporting information), such a shift in water wettability of the NP is not permanent. Instead, it regains the embedded water wettability after air-drying, as shown in Figure 2G. The cycle was repeated 20 times without having any permanent changes in the water wettability (Figure 2G). To understand this behavior of prepared NP, its topography was analyzed with FE-SEM before and after exposure to water for 60 minutes. No noticeable change in topography was observed (Figure 2H), suggesting a minimal impact of wettability adaptation on the topography of the prepared NP. While this, the FT-IR spectra (Figure 2I) of the same NP recorded before and after exposure to water for 60 minutes revealed no change in the proportion of characteristic signature for the amide I band (1648 cm^{-1}) and amide II (1535 cm^{-1}) band of BSA and ester carbonyl stretching (1736 cm^{-1}) from the selected crosslinker, suggesting a minimal alteration in chemical composition. Thus, the wettability adaptation by the prepared NP lacks any permanent alteration of either topography or chemistry. Eventually, such material can be reused for multiple cycles. Thereafter, these differently modified NPs were employed to prepare liquid marbles (LMs).

The wrapping of adequately modified NPs on water droplets (10 μL) provided LMs (Figure 3A, Movie 1), where the contact angle of beaded LMs on hydrophilic glass surfaces exhibited a distinct static contact angle (denoted as θ_{LM}), depending on the length of hydrocarbon chains (n = 3 or 18; Figure 3A) of modified NPs. The θ_{LM} gradually improved from 146° to 169° with increasing the chain length (n) from 3 to 18 of the selected modifiers because of the elevation in hydrophobicity of the modified NP, as shown in Figure 3B and Figure S6, supporting information. These LMs, derived from NPs decorated with distinct hydrocarbon moieties, either automatically break or buckle while beaded on a bare glass surface for a certain duration, as depicted in Figures 3C and 3D. We observed that LMs with relatively shorter hydrocarbon chains (i.e., $n < 6$) encounter automated breakage to release inner liquid (Movie 2). In contrast, LMs with hydrocarbon chains of $n \geq 6$ do not break; rather, they buckled due to the evaporation of encapsulated water (Figure S7, supporting information and Figure 3C). In the plot of Figure 3D, the green region depicts the breaking of LMs, whereas the blue and red areas indicate the not-breaking and the complete inner liquid evaporation, respectively. The time taken by the LMs to break on the glass surface was noticed to be gradually increased from 5 to 25 min on changing the carbon chain length from 3 to 5, as shown in Figure 3D. There are two competitive factors: a) adaptation of water wettability by modified NPs and the

evaporation of the encapsulated water of LMs. The faster adaptation of water wettability hydrophilizes the LM shell (for modification with $n < 6$; Figure 3C), and it breaks from the bottom part, which is in contact with the hydrophilic solid surface as shown in digital images in Figure 3E, highlighted with green background. The white arrow in the dotted red box indicates the released water from LM on the bare glass. We observed that the LMs derived from the powder, with a faster rate of hydrophilization (that is, the larger β), break faster. However, in the case of the LMs having chain length $n \geq 6$, the wettability adaptation time is slower than the evaporation of the inner liquid. So, the encapsulated water evaporates from LMs before modified NPs experience a significant water wettability change, resulting in no breakage of these LMs. The representative images in Figure 3E, highlighted with the blue and red backgrounds, depict the scenario where LMs with $n = 10$ and 18 do not break even after 60 and 120 minutes, respectively. Instead, they are found with less or more buckling of their shells. Thus, LMs prepared with NPs having three different chemical modifications ($n = 3$, 4, and 5) displayed an automated breaking phenomenon with a window of breaking time from 5 to 25 minutes. While the automated breaking of LMs on the water pools has been demonstrated recently through the formation of liquid bridges [32], the report on the release of inner liquid on a solid surface, without any external intervention, is unprecedented.

LMs derived from the NP powders modified with propyl, butyl, and pentyl remained appropriate for releasing inner liquid on a solid surface automatically. Hence, the control over the timing of the automated breaking of LMs is limited to three different options. As an alternative approach, we have introduced a strategy of mixing powders of NPs that were individually decorated with propyl ($n = 3$) and octadecyl ($n = 18$) moieties, where NPs with propyl modification display much faster adaptation with respect to NPs having octadecyl ($n = 18$) modification. NPs with octadecyl ($n = 18$) and propyl ($n = 3$) modifications are mixed with different weight proportions, and each resultant mixture of NP powders is represented with Φ, i.e., the fraction of mass (W_n) of NP having propyl ($n = 3$) moiety $W_{n=3}$ with respect to the total mass of the mixture $W_{n=18} + W_{n=3}$. After mixing, we get different mixtures of powders, where Φ values gradually vary from 0 to 1. The water repellence of the resultant mixtures of NPs gradually decreased from 156° to 140° with increasing Φ from 0 to 1, as accounted in Figures S8 and S9 (supporting information), as the content of NPs decorated with propyl moiety gradually increased. This additivity allows the fine-tuning of the lifetime of LMs on the bare glass surface. We achieved an automated breakage of LMs for $\Phi = 0.40$ to 1, and for $\Phi = 0$ to 0.25, the LMs do not break but rather buckle due to evaporation of the inner liquid (Figure 4A). The wettability of these powders of different mixtures was characterized by measuring the water CA (θ_w), which shows an increasing trend with the elevating the content of NP embedded

with longer (n = 18) alkyl chains in the mixtures (Figure S8 and S9, supporting information). Furthermore, the wettability adaptation by these mixtures has been investigated by monitoring the change in the θ_w with time (Figure S10A, supporting information). The cosine of the θ_w with the time for different mixtures shows the faster adaptation speed with a higher proportion of NP powder having shorter alkyl chains (n = 3; Figure S10B, supporting information). The hydrophilization rate β for the different mixtures was obtained from the Malthusian contact model (Figure S11, supporting information). We found the hydrophilization rate β linearly increased with the fraction of the mixture, that is $\beta \sim \Phi$. This means a faster trend with the increase of the content of NPs, which has shorter-alkyl chains (n = 3) in the selected mixtures of NPs (Figure 4B). Thus, the additivity is allowed for the hydrophilization speed, and from Equation (2), we obtain:

$$\beta \sim \sum W_n n^{-1} / \sum W_n \quad (3)$$

We hypothesized that on the molecular scale, the hydrocarbon tails associated with NPs played an important role in the water infiltration rate and so water adaptation, as schematically depicted in Figure 4C. The powder with Φ = 0.85, having dominance of shorter hydrocarbon chains, displayed a significant change in θ_w from 142°to 93° within 30 minutes (Figure S10, supporting information) due to relatively fast infiltration of water through these short chains, where a few of long hydrocarbon moieties act oppositely—and prevents complete wetting even after 30 minutes. Thus, the long hydrocarbon chains act as a slow adaptation factor in the wetting process. As a consequence, the mixture with Φ = 0.25 having the dominance of long hydrocarbon chains restricts the penetration of water, and thus, the alteration of θ_w, even after 30 minutes, was noticed to be minimal (Figure S10A, supporting information).

The LMs were derived from these mixtures (from Φ = 0 to 1) of two distinct NPs that are separately decorated with a propyl (n = 3) and octadecyl (n = 18) moiety using a water droplet (10 μL) (Figure S12, supporting information). The static contact angles of these LMs (θ_{LM}) demonstrate a decreasing trend with an increase of the Φ values (Figure 4D). The mass of the LM shell on the same volume of the water droplet was gradually depleted by decreasing the Φ from 1 to 0 (Figure S13, supporting information). We noticed a similar trend for shell thickness and porosity of the prepared LMs while altering Φ from 1 to 0 (Figure S14 and S15, supporting information). The gradual change in their appearance and contact angles with time on the glass substrate was monitored and accounted for in Figures S16 and S17 (supporting information). Depending on the Φ of the selected mixture of NP powders, respective LMs either encountered automated breaking or only bucking (Figure 4E). In the plot of Figure 4E, the green region refers to the breaking of LMs, and the blue and red regions denote either not-breaking or buckling after complete evaporation of inner liquid for respective LMs. The digital images

in Figure 4F account for the representative images of LMs illustrating all three situations (Figure 4F). This particle mixing approach enables a fine-tuning of the lifetime of these LMs, where the automated breakage of the LMs was noticed for five different lifetimes (Φ from 1 to 0.4) with a time range of 5 to 25 minutes. Fine tailoring of the composition of mass fraction of selected modified NPs may provide a basis to fine-tune the lifetimes of LMs further.

The LMs derived from the short-alkyl chain modifications or mixture of NP with a higher proportion of the short-alkyl chain components have a tendency to break automatically when put on a hydrophilic solid surface and release their inner liquid from their contact point with the surface. In fact, the time to break LMs on a hydrophilic substrate can be controlled by varying the carbon chain length (n) and mixture ratio (Φ) of selected NPs. The unique ability of these LMs has been strategically applied to achieve their automated coalescence while beaded on a superhydrophobic solid surface (which was prepared following a reported procedure [33]). As a proof of concept demonstration, two LMs derived from NP powders having n = 3 (Φ = 1) were beaded on a superhydrophobic substrate, maintaining physical contact with each other, as shown in Figure 5A. They start coalescing through points of contact and finally become a single marble within 2.5 minutes (Movie 3). Superhydrophobic substrate prevents the breaking of LMs; rather, LMs coalesced automatically after a certain time in the absence of any external stimuli. During the coalescence of two LMs, a liquid bridge forms at the point of contact due to the capillary force of water penetrating through covered powders, as illustrated in Figure 5B. A further experiment was performed to fix a coalesced LM with super glue [34, 35-38] prior to manually opening two ends of the LMs. No blockage at the place of coalescence was noticed; rather, the middle portion of the coalesced LM remained empty and hollow (Figure S18, supporting information), supporting the formation of a channel between coalesced LMs. Thereafter, two LMs with identical Φ values were allowed to coalesce, where Φ was gradually altered from 0.40 to 1. The coalescence time decreases with an increase in the Φ values (Figure 5C). So, the LMs with greater proportions of shorter alkyl chains tend to coalesce faster. In another scenario, two LMs with different Φ values also coalesced. In this experimental set-up, Φ of one LM was kept unaltered (Φ = 1) while the Φ of other LM was altered gradually from 0.40 to 0.85. The coalescence time decreases with an increase in the Φ of the other LMs (Figure 5D). But, here, we observe an interesting result: two LMs of the same Φ (i.e., 0.70) coalesced three times slower while compared with coalescence between two LMs with different Φ of 0.70 and 1. This phenomenon has been explained by our model in Figure 5B. Since these LMs have a higher rate of adaptability for water, water penetrates through the powder and becomes wetted over time, depending on the modifications. For the coalescence of the same LMs, since the rate of hydrophilization (β) is the same for both the powders, the capillary force for water

penetration through the shells is the same. But for the coalescence of two different LMs, when one of the marbles is made out of powder with a higher β value than the other, the capillary force for the penetration of water through the shells is higher for the LM having a higher β value. Thus, water penetrates through the shell of that LM and goes into the other LM having slower water penetration speed to form a liquid bridge. Thus, the coalescence of LMs having $\Phi = 0.70$ with another LM having $\Phi = 1$ is faster than the coalescence of two LMs having the same Φ, i.e.,0.70. On comparing the LM coalescence time with the shell thickness of LM prepared with particle mixtures of different Φ and adaptation rate (β) of these particle mixtures, we noticed that coalescence time decreased with increasing β even though the shell thickness of LM increased with Φ as shown in Figure S19. This result indicates that the impact of β dominates over the shell thickness of LMs towards the coalescence time. However, this study failed to explain the exact relation between shell thickness and coalescence time. Thereafter, we demonstrated the coalescence of two LMs having differences in the volume of inner liquid (Figure 5E and Figure S20, supporting information), where the Φ remained unaltered. In this experiment, the volume (denoted as Ω) of one LM was 30 µL, and the Ω of the other LMs was varied from 5 µL to 20 µL. However, irrespective of the difference in the volume of LMs, we get the same coalescence times (Figure 5F). Moreover, the diffusion of the molecules (i.e., methylene blue) was noticed against the concentration gradient from one LM to another LM (Figure 5G) as the coalesced LMs formed a liquid bridge.

Next, multiple LMs were arranged in different shapes, including lines, triangles, and circles, to demonstrate an organized coalescence of LMs of the same Φ values (Figure 5H, 5I, 5J, Figure S21, supporting information). One of the NP powders was modified with a dye (Nile red) for facilitating the visual inspection. Also, we have successfully demonstrated the patchwork of LMs having different Φ (Figure S22, supporting information). In this relevance, a programmed cascade coalescence of LMs was demonstrated in Figure 5K, where we have prepared LMs of different Φ by encapsulating aqueous solutions of different dyes for improved visual inspection. At the center, a LM with Φ of 0.85 (Ω = 40 µL) was placed, and other LMs (Ω = 20 µL) with Φ of 1, 0.85, 0.70, 0.55 were kept around it in a clockwise manner. As time proceeds, LMs coalesced one after another in a clockwise manner (Figure S23, supporting information and Movie 4). On coalescence, we noticed diffusion and mixing of different dyes at the large LM placed at the center. It is worth to mention that the coalescence time decreases with the increase in humidity (Figure S24), likely due to the faster adaptation of the LMs in highly humid environments. Moreover, the chemically modified NP powders remained capable of automated coalescences even after aging for six months, as shown in Figure S25. This study suggests the

long-term stability of these modified NPs. It is likely due to the covalent modification of reactive nanoparticles with selected alkyl amines through a 1,4-conjugate addition reaction.

In the last section, we demonstrated an automated and programmed coalescence of LMs without requiring any external stimuli, where we can program their coalescence time by changing the Φ of the powder mixture. Using this feature, here we attempted to depict a cascade chemical reaction by programming the coalescence of LMs loaded with mutually reactive reactants and reagents. In this relevance, we have selected a Schiff base reaction to perform between salicylaldehyde (R-1) and propyl amine (R-2), followed by a reduction of the synthesized imine product (labeled as P-1) with a reducing agent $NaBH_4$ (R-3) to get a reduced product (denoted as P-2; Figure 6A). Three LMs in the order of Φ = 1.0, Φ = 1.0, and Φ = 0.7, each containing R-1, R-2, and R-3, respectively, were kept in contact with each other on a superhydrophobic substrate. Since LM with Φ = 1 tends to coalesce faster than the LM having Φ of 0.70, the two LMs having Φ of 1 coalesce first, resulting in the formation of a yellow-colored imine product (P-1), which after second coalescence with the LM of Φ = 0.70 results in the reduction of the imine bond, giving a colorless reduced product (P-2) (Figure 6B, Movie 5). For the control study, we demonstrated the simultaneous coalescence reaction, where we put three LMs in the order of Φ = 1, Φ = 0.70, and Φ = 1, each containing R-1, R-3, and R-2, respectively, on a superhydrophobic substrate. The LM with Φ of 0.70 coalesces with the other two LM having Φ of 1 at the same time, so R-1 reacts with R-3, resulting in the reduction of salicylaldehyde to give colorless silyl alcohol (P-3), and remains inappropriate to react with propyl amine (R-2). So, we have a mixture of R-2 and P-3 in the final coalesced marble. Due to the simultaneous coalescence of the LMs, no Schiff base reaction took place. As a consequence, no color change was noticed (Figure 6C, D). The products, because of the cascade coalescence of LMs, were characterized with FT-IR and ^{1}H NMR spectra. The appearance of the new IR peak at 1656 cm^{-1} due to the -C=N bond and simultaneous depletion of the carbonyl peak of salicylaldehyde at 1720 cm^{-1} confirms the imine bond formation in P-1 through mutual reaction between amine and aldehyde groups. The IR spectrum of the P-2 shows the disappearance of the -C=N peak at 1656 cm^{-1}, confirming the reduction of the imine bond (Figure 6E). The product (P-2) formed because of the cascade coalescence LMs was further characterized by ^{1}H NMR (Figure 6F), where peaks at δ = 0.88 (3H, t), δ = 1.48 (2H, m), δ = 2.48 (2H, t), and δ = 3.82 (2H, s) ppm revealed the existence of the aliphatic protons a, b, c and d respectively. Moreover, the ^{1}H NMR signatures at δ = 7.04, 6.69 ppm belong to four aromatic protons (e, f, g, h). Similarly, resultant products, because of the simultaneous coalescence of LMs, were characterized by ^{1}H NMR (Figure 6G). The P-3 shows a characteristic ^{1}H NMR signature at δ = 4.56 (2H, s) for proton i and δ = 6.91, 6.80, 6.52, 6.44 ppm for the four

aromatic protons ii, iii, iv and v. While this, the ^{1}H NMR spectra also contain the peaks for the protons of aliphatic hydrogens of R-2 at δ = 0.84 (t), δ = 1.33 (m), and δ = 2.48 (t) ppm for protons vi, vii and viii respectively. Thus, the final reaction mixture contains both R-2 and P-3. Such cascade chemical reaction based on programmed coalescences of LMs was also successfully demonstrated using another set of reactants, lead nitrate ($Pb(NO_3)_2$), potassium iodide (KI), and sodium thiosulfate ($Na_2S_2O_3$) using the set of LMs (Figure S26, supporting information).

Thereafter, a gas evolution reaction was also performed by automated coalescence of the LMs. For this purpose, we chose a redox reaction between $KMnO_4$ and H_2O_2, resulting in the formation of MnO_2 and O_2 gas evolved in the process (Figure 6H). We took $KMnO_4$ and H_2O_2, each in separate LMs having the same Φ (i.e., 1.0), and put them in physical contact on a superhydrophobic substrate. Since the LMs coalescence took place because of adaptive wettability, a thin water layer formed around the interior of the marble shell, and the O_2 gas formed due to the reaction could not cross the water layer that acts as a barrier to form gas marble.[39] So, O_2 gas is stored locally inside the LM. In the end, we have a marble with both liquid and gas inside it, namely a "Janus liquid/gas marble". Due to the accumulation of O_2 gas, it also gets bigger in size (Figure 6I, Movie 6). For the control experiment, we took two $\Phi = 0$ LMs with a very slow adaptability toward the water. So, these LMs do not coalesce automatically if we put them in contact with a superhydrophobic substrate. Hence, we mechanically coalesce them with the spatula. After coalescence, the reaction took place between $KMnO_4$ and H_2O_2, and the brown color MnO_2 formed, where O_2 gas escaped from the LM. Since there is no adaptive wetting, there is no barrier of water layer forms, and gas can easily diffuse out of the shell of selected LMs (Figure 6J, Movie 7).

Conclusion:

This work reports LMs that can coalesce in each other or release the inner liquid with preprogrammed time. Such time-programmed design of functional LMs may open a new paradigm in droplet manipulation. The LM function is achieved by the chemical modulation of the adaptation time of the NPs from hydrophobic to hydrophilic. Since the advocation of the adaptive wetting theory in 2018 [31], a fundamental understanding of the molecular effect on its adaptivity has been unclear. This work clarified that (1) adaptation speed, denoted as hydrophilization rate, is decided by the alkyl chain length, and (2) additivity is allowed to regulate adaptation speed. We believe this work contributes to the development of functional

soft materials engineering and understanding of interfacial science. Moreover, the droplet cascade chemical reaction and generated Janus liquid/gas marble opens a new concept in droplet/bubble science. Previously, controlled coalescences of droplets through the strategic use of reactive surfactants provided a basis for droplet manipulation and assembly.[40-44] In this context, the current approach of automated and programmed coalescence of LMs is likely to open up various other possibilities to derive functional materials and interfaces. Currently, the existing modified NPs are limited to aqueous systems only. However, we believe this work can be extended to low surface tension liquid by fluorinating the hydrophobic moieties of NPs to achieve the adaptive LMs for non-aqueous systems.

Experimental Section

Fabrication of LMs embedded with adaptive wettability: The chemically reactive NP of BSA was derived by applying the desolvation method, followed by its covalent crosslinking with 5Acl. Thereafter, it was post-modified with selected alkyl amines, i.e., propyl amine, butyl amine, pentyl amine, hexyl amine, octyl amine, decyl amine, octadecyl amine through 1,4-conjugate addition to achieve adaptive hydrophobic NPs. LMs embedded with adaptive wettability were derived from these post-modified NPs to demonstrate the automated coalescence of LMs, cascade chemical reactions, etc. Reactive and modified NPs were characterized using conventional techniques, where KRUSS Drop Shape Analyzer DSA25 was used to investigate water wettability, the morphology of NPs was investigated with FE-SEM, and ATR-FTIR was applied to reveal postchemical modifications. All digital images and videos were captured with a Nikon Coolpix B700 digital camera. NMR spectra were recorded by using a Bruker 400 MHz NMR spectrometer. Further, detailed procedures are available in the supporting information section.

Statistical Analysis: All the experiments were performed in triplicates. Results are presented as mean ± SD.

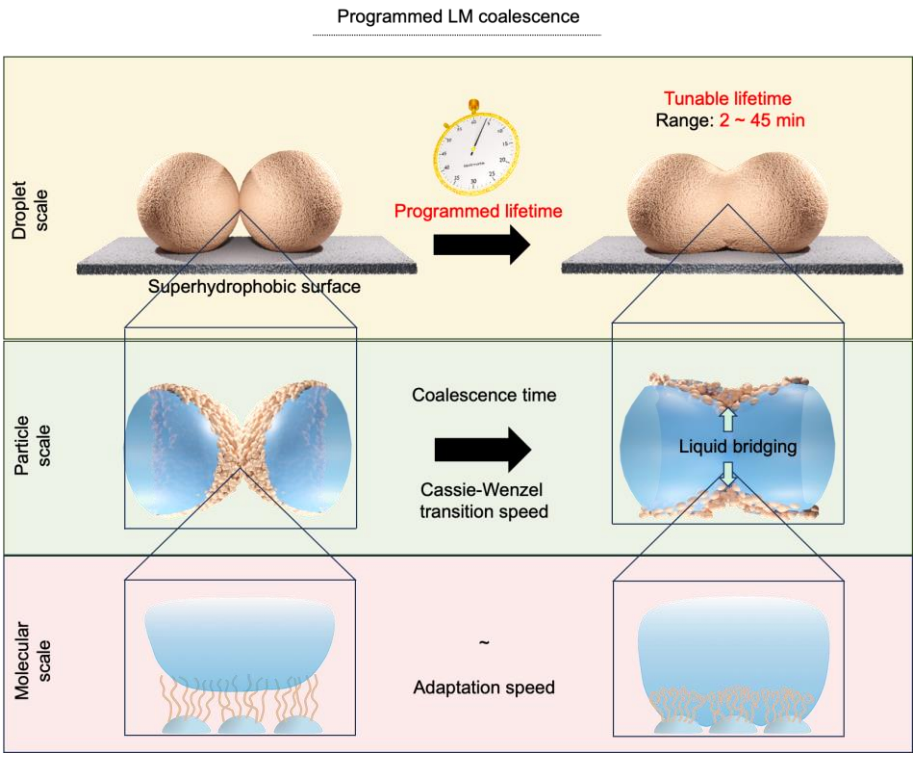

Scheme 1: Scheme depicting the automated coalescence of LM on a superhydrophobic surface with a programmed coalescence time, where Cassie-Wenzel transitional speed in particle scale and water adaption in molecular scale influenced the coalescence time of LMs.

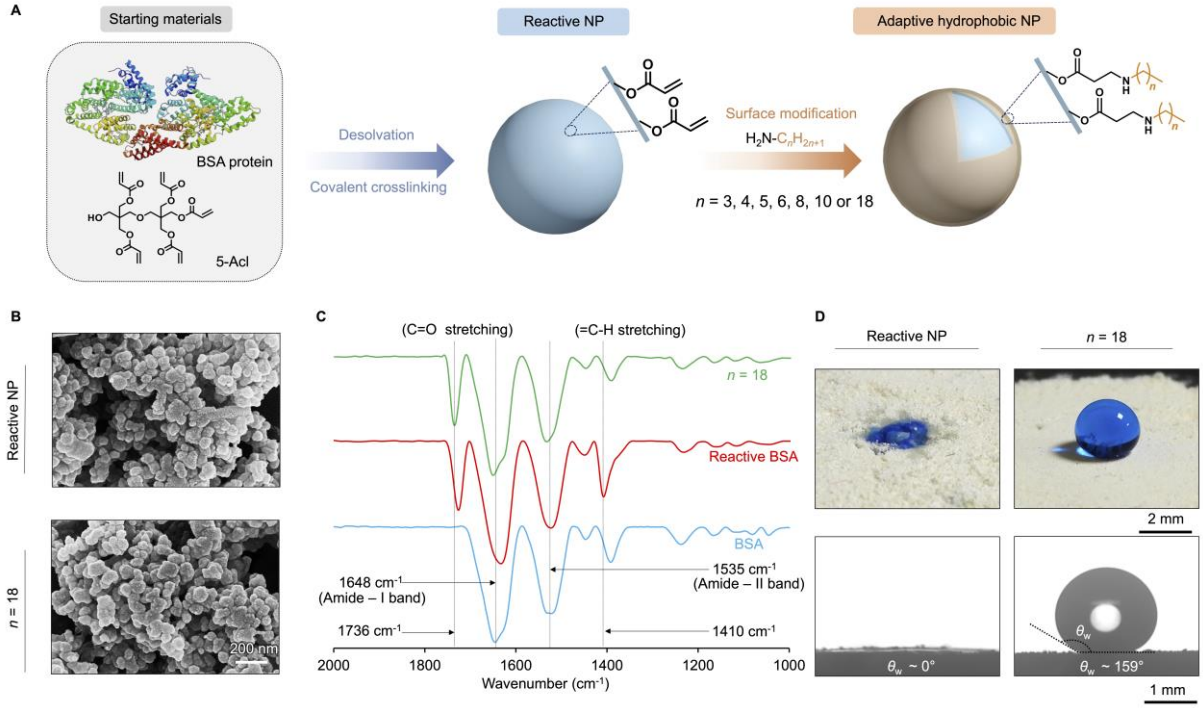

Figure 1. A) Accounting selected starting materials: bovine serine albumin (BSA) and dipentaerythritol penta-acrylate (5-Acl) for preparing reactive nanoparticles (NP) of BSA having residual acrylates. Its subsequent surface modification with alkyl amines having different chain lengths through a 1,4-conjugate addition reaction allowed it to achieve adaptive hydrophobic NPs. B) Field emission scanning electron microscopic (FE-SEM) images of the reactive NPs and octadecyl-modified NPs (n = 18). C) Attenuated total reflection-Fourier transform infrared (ATR-FTIR) spectra of the BSA, reactive NPs of BSA, and octadecyl-modified NPs (n = 18). D) Digital (top panel) and contact angle (bottom panel) images demonstrating the change in water wettability on powder bed for reactive NPs and octadecyl-modified NPs (n = 18). The static contact angle on the powder bed is illustrated by θ_w.

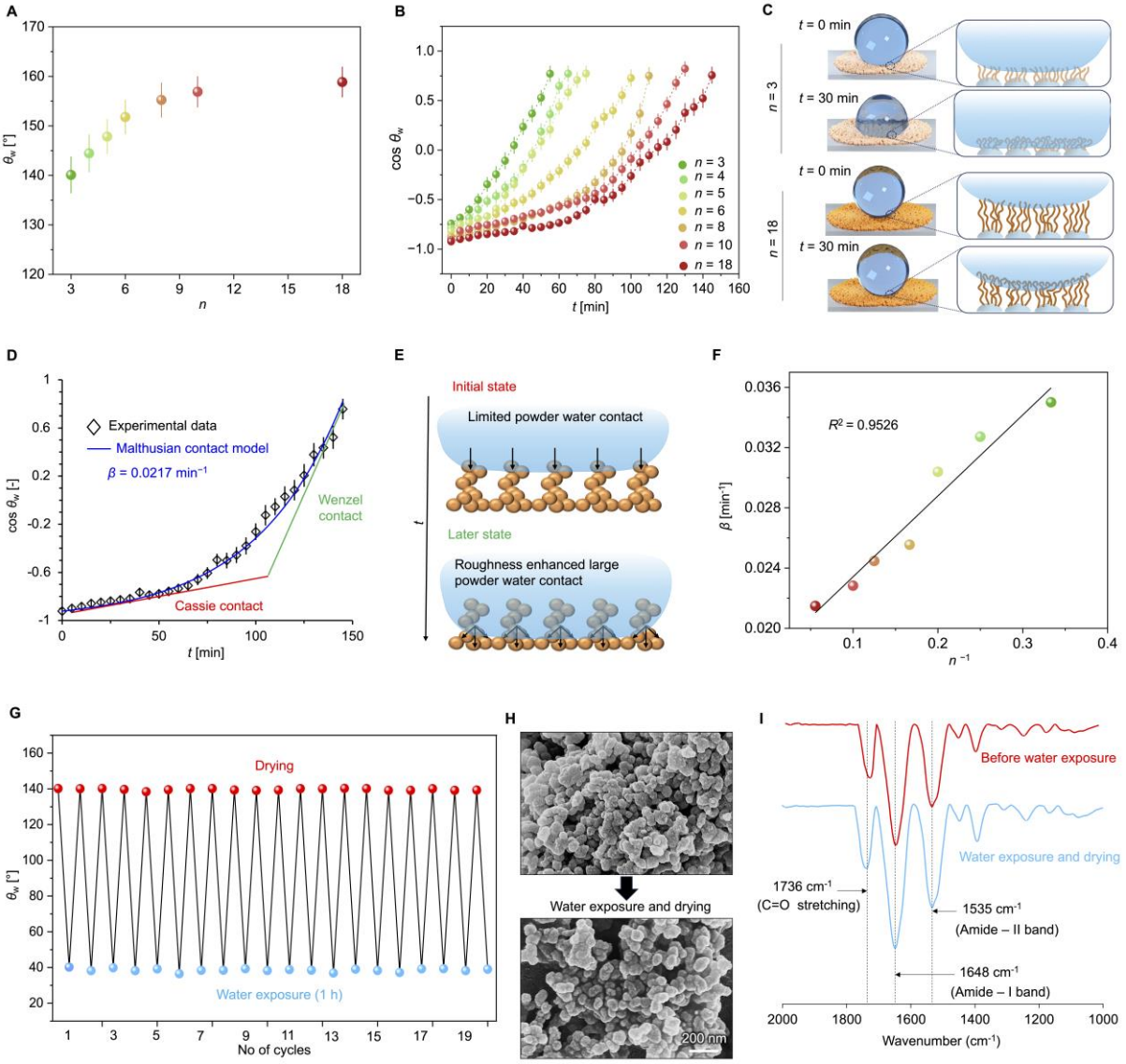

Figure 2. A) Plot accounting for the apparent contact angle (θ_w) at t = 0 on the powder bed of NP modified with different alkyl amines (from n = 3 to 18). B) Plot illustrating the change in wetting behavior of water on a powder bed of different amine modifications with time. C) Schematics illustrating the water-wetting behavior of NPs with n = 3 or 18 before and after 30 min. The right side is the magnified images demonstrating the wetting behavior on a molecular scale. D) Accounting experimental results and Malthusian contact model for wetting behavior with time for NP with n = 18. E) Schematics illustrating the water ingression behavior with time for modified NPs. F) Plot accounting for the change in the rate of hydrophilization (β) of NPs with n. G) Plot depicting the changes in θ_w for NPs with n = 3 before and after exposure to water for 1 hour for 20 repetitive cycles. H-I) FE-SEM images (H) and ATR-FTIR spectra (I) of NPs with n = 3 before and after exposure to water for 1 hour. Results are presented as mean ± SD, where sample size, n = 3.

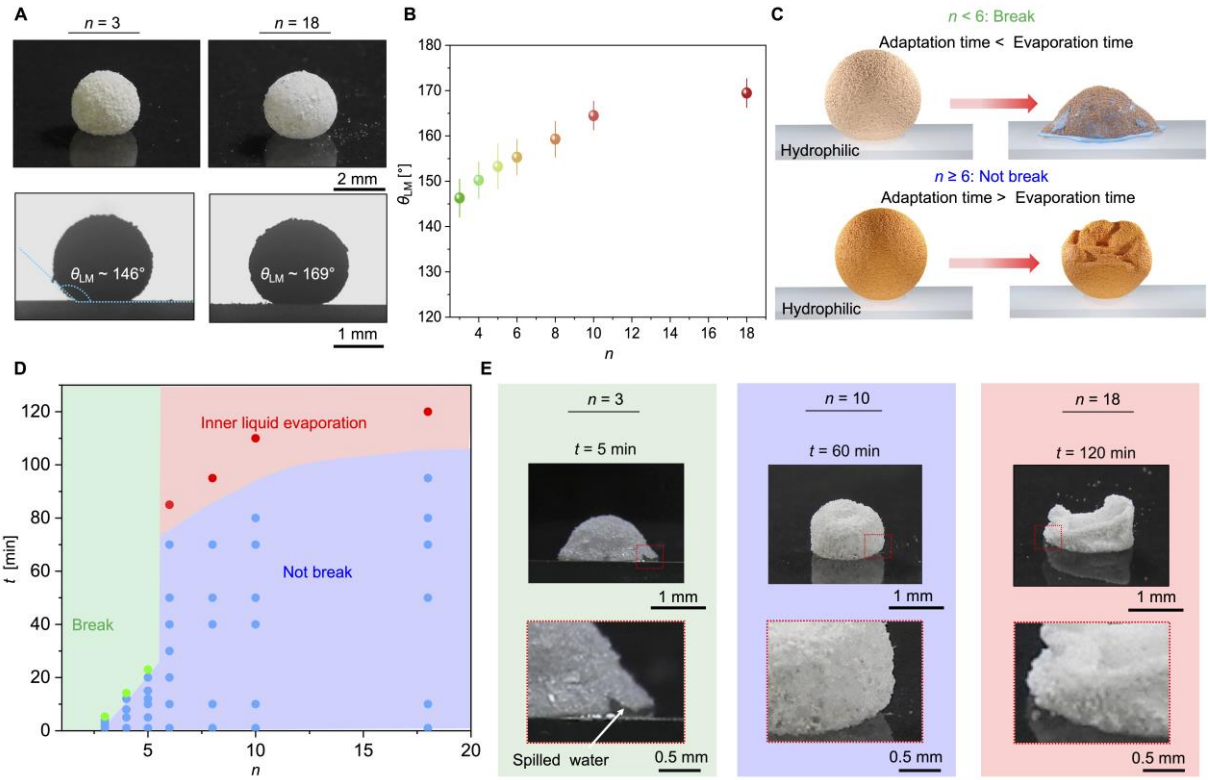

Figure 3. A) Digital images (top panel) and contact angle images (bottom panel) of LMs derived from NPs decorated with different alkyl chains: n = 3 and n = 18. The static contact angle of the LM is represented as θ_{LM}. B) Plot accounting for the change in θ_{LM} with alkyl chain, n (from 3 to 18). C) Schematics illustrating the fate of LMs on a hydrophilic solid surface depending on the associated alkyl chain. LMs break when $n < 6$, and no breakage of LMs was noticed for $n \geq 6$. D) Plot accounting for the lifetime of LMs on the solid surface depending on alkyl chain, n, where green, blue, and red regions denote break, not break, and the complete evaporation of LMs. E) Digital images showing the behavior of LMs on a hydrophilic glass surface for different n. The top panel represents the digital images of the LMs, and the bottom panel represents magnified images to illustrate the breaking of LM (green region, n = 3), no breakage of LM (blue region, n = 10), and the complete evaporation of LM (red region, n = 18). Results are presented as mean ± SD, where sample size, n = 3.

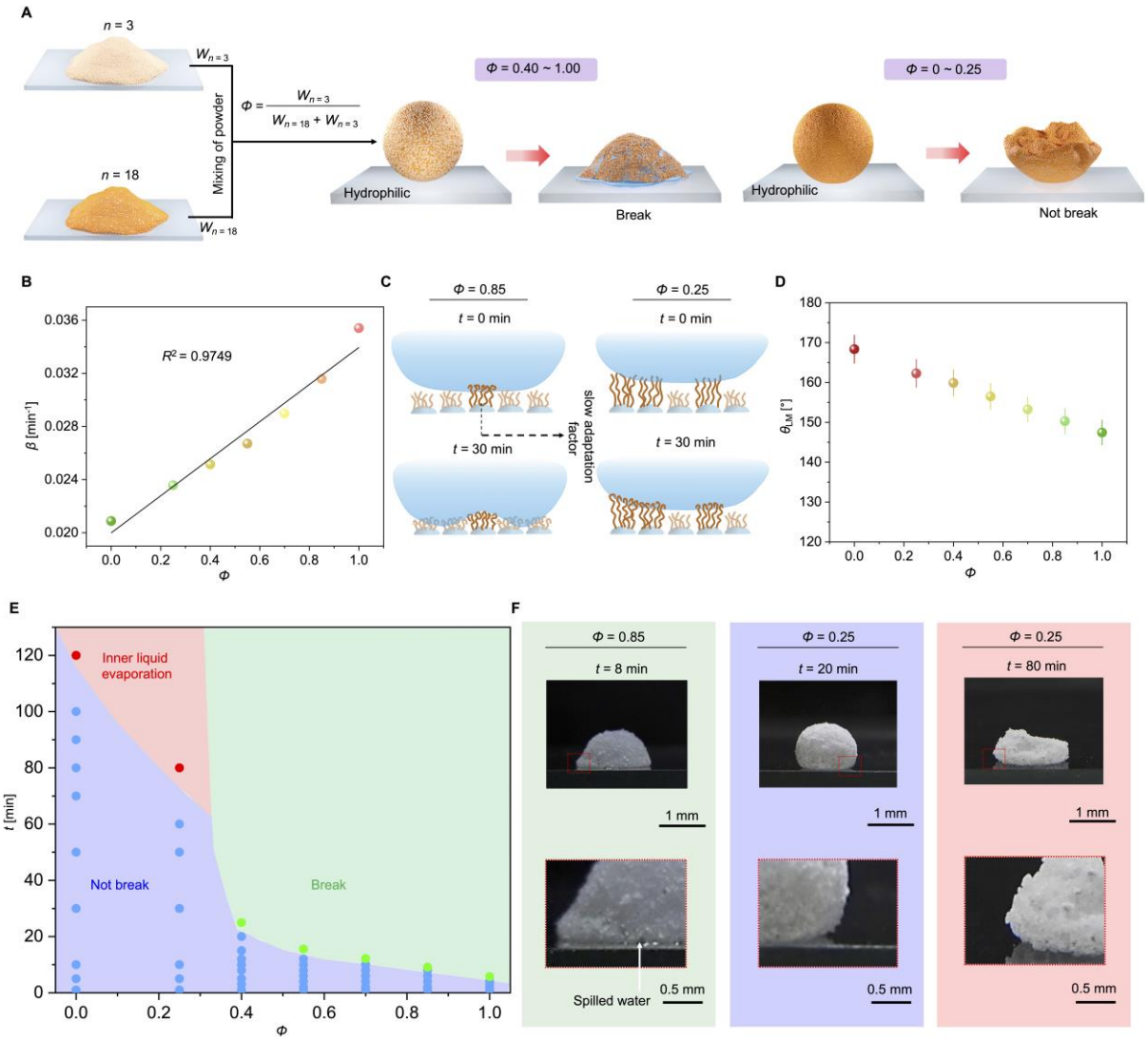

Figure 4. A) Schematics account for the mixing of NPs associated with two distinct chemical modifications: n = 3 and n = 18, where the mixture of different weight proportions is denoted by Φ. LMs derived from this resultant powder mixture having different Φ displayed different behaviors while beaded on a hydrophilic solid surface. B) Plot accounting for the change in the rate of hydrophilization (β) with different Φ. C) Schematics illustrating the wetting behavior of mixtures on a molecular scale, for Φ = 0.85 and Φ = 0.25. D) Plot accounting for the change in θ_{LM} for different mixtures having Φ from 0 to 1. E) Plot accounting for the lifetime of LMs derived from mixtures having Φ from 0 to 1 while beading on a solid surface, where green, blue, and red regions depict the breaking of LMs, not breaking of LMs, and the buckling of LMs. F) Digital images illustrating the behavior of LMs beaded on a hydrophilic glass surface, where the top panel represents the digital images of the representative LMs, and the bottom panel accounts for magnified images for breaking of LM (green region, Φ = 0.85), no breakage of LM (blue region, Φ = 0.25) and the buckling of LM (red region, Φ = 0.25). Results are presented as mean ± SD, where sample size, n = 3.

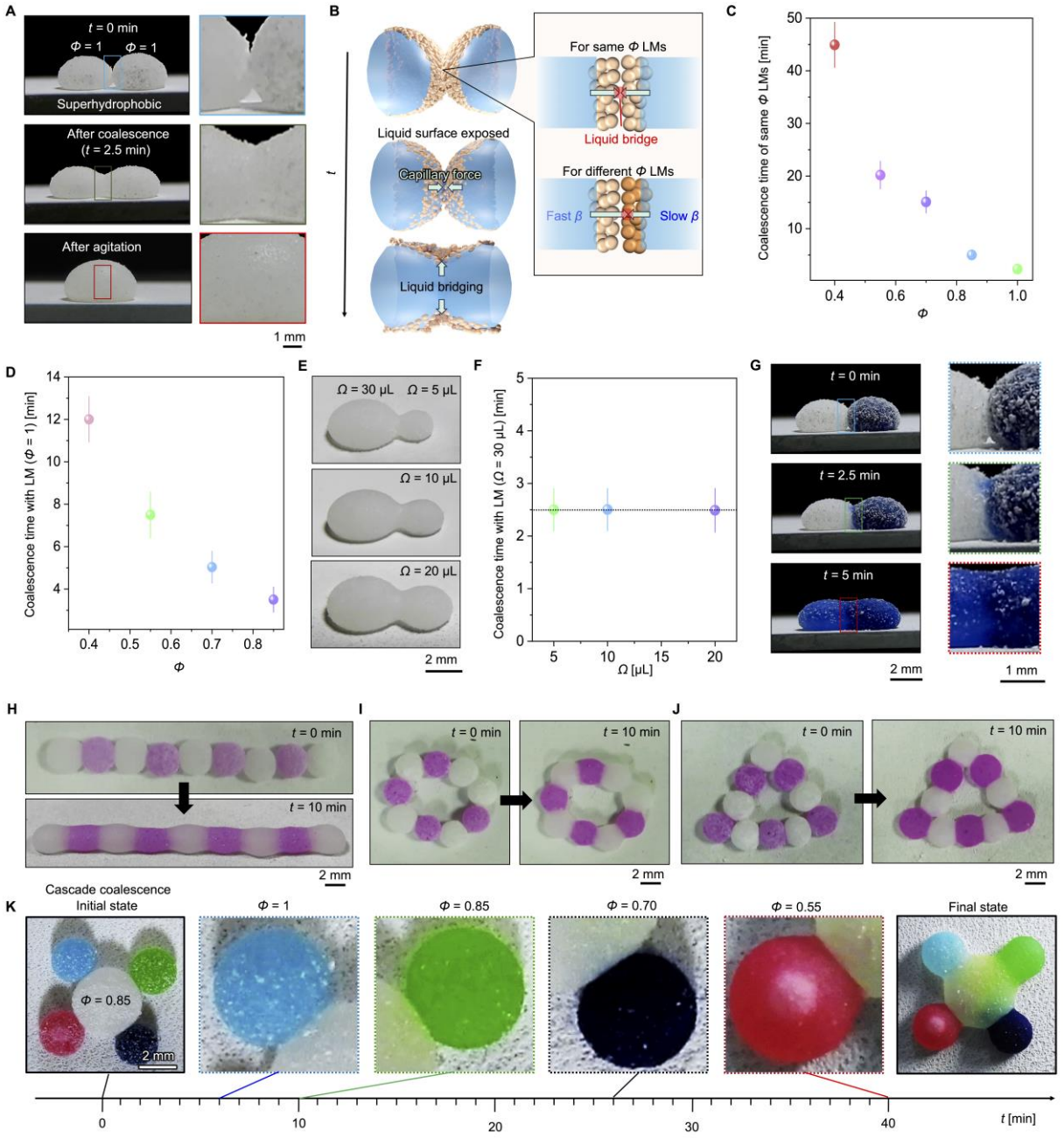

Figure 5. A) Digital images depicting automated coalescence of LMs having volume (Ω) *of* 20 μL) and Φ = 1 on a superhydrophobic surface, the corresponding zoomed images illustrating the physical changes at the point of contact between two LMs. Agitation of coalesced LMs altered its shape. B) Schematics depicting the automated coalescence of LMs through the formation of a liquid bridge and the rate of coalescence for LMs having the same and different Φ values. C-D) Plot of the coalescence time of LMs having the same (C) and different (D) Φ values. E) Digital images of coalesced LMs having different Ω. F) Illustrating the same coalescence time for a given Φ (i.e., 1), irrespective of Ω. G) Digital images of automated coalescence of LMs with Φ = 1 showing diffusion of dye from one LM to another on coalescence. H-J) Digital images illustrating the coalescence of multiple LMs on the

superhydrophobic interface in different shapes, including line (H), circle (I), and triangle (J). K) Digital images exhibiting programmed cascade coalescence of LMs with time, where LMs are loaded with different color dyes for improved visual inspections. Results are presented as mean ± SD, where sample size, n = 3.

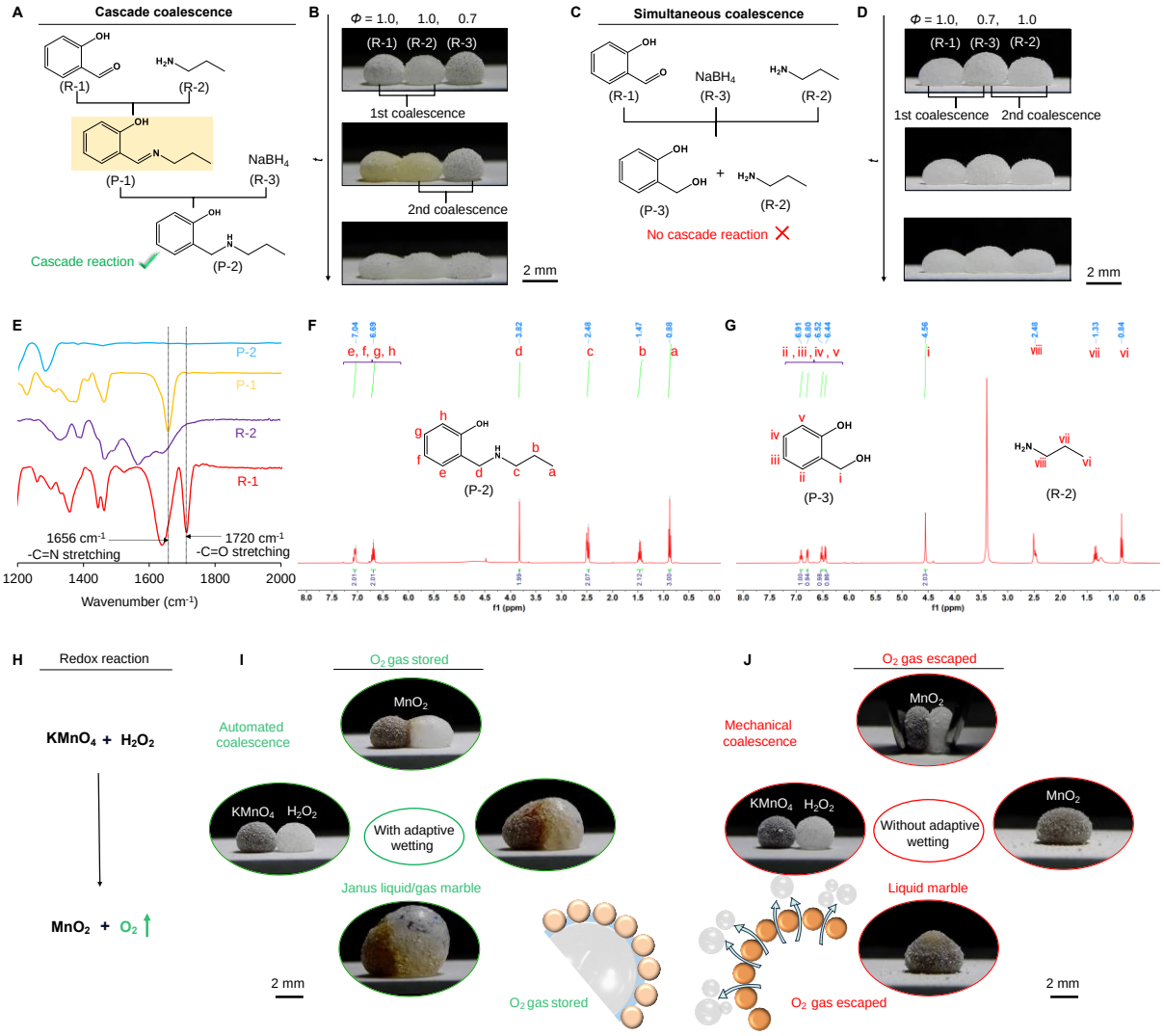

Figure 6. A-D) Demonstration of the programmed cascade chemical reaction through automated coalescence. A) Reaction scheme of the programmable cascade reaction of salicylaldehyde (R-1) and propyl amine (R-2), giving the Schiff base (labeled as P-1). Its reduction by sodium borohydride (R-3) provided 2-((propylamino)methyl)phenol (denoted as P-2). B) Digital images showing the programmed cascade chemical reaction, where coalescence of the first two LMs from the left side yielded yellow-colored P-1, and its further coalescences provided colorless P-2. C) The reaction scheme illustrates the consequence of the simultaneous coalescence of LMs having salicylaldehyde (R-1), sodium borohydride (R-3), and propyl amine (R-2). The reduction of salicylaldehyde gives salicyl alcohol, which does not react with propyl amine. D) Digital images depicting the simultaneous coalescence reaction, where the

arrangement of LMs is just altered. E) ATR- FTIR spectra of R-1 (red), R-2 (purple), P-1 (yellow) and P-2 (blue). F-G) NMR spectra of the final products because of the cascade (F) and simultaneous (G) coalescence of LMs loaded with R-1, R-2, and R-3. H) Reaction scheme for the redox reaction between $KMnO_4$ and H_2O_2, resulting in MnO_2 and O_2 gas formation. I) Digital images illustrating the reaction between $KMnO_4$ and H_2O_2 on the automated coalescence of LMs ($\Phi = 1$), resulting in the formation of O_2 gas, which could not escape from the marble, thereby accumulating inside and forming a Janus liquid/gas marble. J) Digital images showing the reaction of $KMnO_4$ with H_2O_2 by mechanical coalescence of LMs ($\Phi = 0$) resulting in the formation of O_2 gas, which escaped the marble.

References

[1] P. Aussillous, D. Quéré, *Nature* **2001**, *411*, 924.

[2] P. Aussillous, D. Quéré, *Proc. R. Soc. A* **2006**, *462*, 973.

[3] M. Tenjimbayashi, T. Mouterde, P. K. Roy, K. Uto, *Nanoscale* **2023**, *15*, 18980.

[4] B. Wang, K. F. Chan, F. Ji, Q. Wang, P. W. Y. Chiu, Z. Guo, L. Zhang, *Adv. Sci.* **2019**, *6*, 1802033.

[5] Z. Zhao, C. Ling, D. Wang, J.-X. Wang, J. Saczek, S. Pramana, S. Sridhar, J. Shang, B. B. Xu, D. C. W. Tsang, J.-F. Chen, S. Wang, *Small* **2020**, *16*, 2002802.

[6] M. Chen, M. P. Shah, T. B. Shelper, L. Nazareth, M. Barker, J. Tello Velasquez, J. A. K. Ekberg, M.-L. Vial, J. A. St John, *ACS Appl. Mater. Interfaces* **2019**, *11*, 9814.

[7] R. K. Vadivelu, H. Kamble, A. Munaz, N.-T. Nguyen, *Sci. Rep.* **2017**, *7*, 12388.

[8] Z. Liu, T. Yang, Y. Huang, Y. Liu, L. Chen, L. Deng, H. C. Shum, T. Kong, *Adv. Funct. Mater.* **2019**, *29*, 1901101.

[9] Y. Xue, H. Wang, Y. Zhao, L. Dai, L. Feng, X. Wang, T. Lin, *Adv. Mater.***2010**, *22*, 4814.

[10] Y. Chu, Z. Wang, Q. Pan, *ACS Appl. Mater. Interfaces* **2014**, *6*, 8378.

[11] X. Luo, H. Yin, X. e. Li, X. Su, Y. Feng, *Chem. Commun.* **2018**, *54*, 9119.

[12] M. Tenjimbayashi, S. Yamamoto, K. Uto, *Adv. Mater.* **2023**, *35*, 2300486.

[13] M. Anyfantakis, V. S. R. Jampani, R. Kizhakidathazhath, B. P. Binks, J. P. F. Lagerwall, *Angew Chem. Int. Ed.* **2020**, *59*, 19260.

[14] H. K. Lee, Y. H. Lee, I. Y. Phang, J. Wei, Y.-E. Miao, T. Liu, X. Y. Ling, *Angew. Chem. Int. Ed.* **2014**, *53*, 5054.

[15] B. S. Lekshmi, S. N. Varanakkottu, *Langmuir* **2022**, *38*, 11743.

[16] J. C. Gomez, N. S. Vishnosky, S. T. Kim, S. A. Dinca, E. B. Finkelstein, R. C. Steinhardt, *Adv. Funct. Mater.* **2023**, *33*, 2214893.

[17] M. Paven, H. Mayama, T. Sekido, H.-J. Butt, Y. Nakamura, S. Fujii, *Adv. Funct. Mater.* **2016**, *26*, 3199.

[18] L. Zhang, D. Cha, P. Wang, *Adv. Mater.* **2012**, *24*, 4756-4760.

[19] X. Fu, Y. Zhang, H. Yuan, B. P. Binks, H. C. Shum, *ACS Appl. Mater. Interfaces* **2018**, *10*, 34822.

[20] M. Tenjimbayashi, S. Samitsu, Y. Watanabe, Y. Nakamura, M. Naito, *Adv. Funct. Mater.* **2021**, *31*, 2010957.

[21] Z. Chen, D. Zang, L. Zhao, M. Qu, X. Li, X. Li, L. Li and X. Geng, *Langmuir* **2017**, *33*, 6232.

[22] Q. Lv, J. Li, R. Wang, L. Zhang, *Part. Part. Syst. Charact.* **2023**, *40*, 2300076.

[23] J. Jin, C. H. Ooi, D. V. Dao, N.-T. Nguyen, *Soft Matter* **2018**, *14*, 4160.

[24] T. C. Draper, C. Fullarton, R. Mayne, N. Phillips, G. E. Canciani, B. P. J. de Lacy Costello, A. Adamatzky, *Soft Matter* **2019**, *15*, 3541.

[25] Z. Liu, X. Fu, B. P. Binks, H. C. Shum, *Soft Matter* **2017**, *13*, 119.

[26] Y. Zhang, X. Fu, W. Guo, Y. Deng, B. P. Binks, H. C. Shum, *Lab Chip* **2019**, *19*, 3526.

[27] Y. Tsumura, K. Oyama, A.-L. Fameau, M. Seike, A. Ohtaka, T. Hirai, Y. Nakamura, S. Fujii, *ACS Appl. Mater. Interfaces* **2022**, *14*, 41618.

[28] Y. Zhao, J. Fang, H. Wang, X. Wang, T. Lin, *Adv. Mater.* **2010**, *22*, 707.

[29] Y. Huang, Y. Luo, W. Zheng, T. Chen, *ACS Appl. Mater. Interfaces* **2014**, *6*, 19217.

[30] B. E. Givens, Z. Xu, J. Fiegel, V. H. Grassian, *Journal of Colloid and Interface Science* **2017**, *493*, 334.

[31] H.-J. Butt, R. Berger, W. Steffen, D. Vollmer, S. A. L. Weber, *Langmuir* **2018**, *34*, 11292.

[32] N. Barman, A. Shome, S. Kumar, P. Mondal, K. Jain, M. Tenjimbayashi, U. Manna, *Adv. Funct. Mater.* **2023**, *33*, 2214840.

[33] K. Maji, U. Manna, *J. Mater. Chem. A* **2018**, *6*, 6642.

[34] N. Vogel, J. Ally, K. Bley, M. Kappl, K. Landfester, C. K. Weiss, *Nanoscale* **2014**, *6*, 6879.

[35] G. Mchale, M. I. Newton, *Soft Matter* **2015**, *11*, 2530.

[36] P. Singha, C. H. Ooi, N.-K. Nguyen, K. R. Sreejith, J. Jin. N. -T. Nguyen, *Microfluid. Nanofluidics* **2020**, *24*, 81.

[37] A. S. Ravi, S. Dalvi, *ACS Omega* **2024**, *9*, 12307.

[38] V. S. R. Jampani, M. Skarabot, U. Mur, D. Baigl, U. Jonas, J. P. F. Lagerwall. M. Ravnik. M. Anyfantakis, *Adv. Mater*. **2024**, *36*, 2408243.

[39] Y. Timounay, O. Pitois, F. Rouyer, *Phys. Rev. Lett.* **2017**, *118*, 228001.

[40] Z. Yang, J. Wei, Y. I. Sobolev, B. A. Grzybowski, *Nature* **2018**, *553*, 318.

[41] F. G. Downs, D. J. Lunn, M. J. Booth, J. B. Sauer, W. J. Ramsay, R. G. Klemperer, C. J. Hawker, H. Bayley, *Nat. Chem.* **2020**, *12*, 363.

[42] K. Feng, N. Gao, W. Li, H. Dong, F. Sun, G. He, K. Zhou, H. Zhao, G. Li, *Small* **2021**, *17*, 2104385.

[43] J. Zhao, Z. Pan, D. Snyder, H. A. Stone, T. Emrick, *J. Am. Chem. Soc.* **2021**, *143*, 5558.

[44] S. Sun, S. Li, W. Feng, J. Luo, T. P. Russell, S. Shi, *Nat. Commun.* **2024**, *15*, 1058.

Acknowledgments

U.M. thanks Science and Engineering Research Board (CRG/2022/000710), DBT(BT/PR45283/NER/95/1919/2022), Ministry of Electronics and Information Technology (no. 5(1)/2022-NANO) for financial support. U.M. thanks CIF, CFN, SHST, and the Department of Chemistry, Indian Institute of Technology Guwahati, for their generous assistance. CRM and D.S. thank UGC for their SRF fellowships.

Author Contributions

U.M. conceived the concept. M.T. performed theoretical studies in the manuscript. C.M. performed the major part of the experimental work with the help of D.S. N.B. and S.K. U.M and M.T. supervised the work. U.M. wrote the manuscript with inputs from other co-authors.

Data availability

The data presented in this article are available from the corresponding authors on reasonable requests.

Competing interests

The authors have no competing interests to declare.

Supplementary information

The online version contains supplementary material.